computers

MDPI

Article

Enhancing Brain Segmentation in MRI through Integration of Hidden Markov Random Field Model and Whale Optimization Algorithm

Abdelaziz Daoudi [1,*] and Saïd Mahmoudi [2,*]

[1] Department of Computer Science, Faculty of Exact Sciences, Tahri Mohammed University, Bechar 08000, Algeria
[2] ILIA Department, Faculty of Engineering, University of Mons, 7000 Mons, Belgium
* Correspondence: daoudi.abdelaziz@univ-bechar.dz (A.D.); said.mahmoudi@umons.ac.be (S.M.)

Abstract: The automatic delineation and segmentation of the brain tissues from Magnetic Resonance Images (MRIs) is a great challenge in the medical context. The difficulty of this task arises out of the similar visual appearance of neighboring brain structures in MR images. In this study, we present an automatic approach for robust and accurate brain tissue boundary outlining in MR images. This algorithm is proposed for the tissue classification of MR brain images into White Matter (WM), Gray Matter (GM) and Cerebrospinal Fluid (CSF). The proposed segmentation process combines two algorithms, the Hidden Markov Random Field (HMRF) model and the Whale Optimization Algorithm (WOA), to enhance the treatment accuracy. In addition, we use the Whale Optimization Algorithm (WOA) to optimize the performance of the segmentation method. The experimental results from a dataset of brain MR images show the superiority of our proposed method, referred to HMRF-WOA, as compared to other reported approaches. The HMRF-WOA is evaluated on multiple MRI contrasts, including both simulated and real MR brain images. The well-known Dice coefficient (DC) and Jaccard coefficient (JC) were used as similarity metrics. The results show that, in many cases, our proposed method approaches the perfect segmentation with a Dice coefficient and Jaccard coefficient above 0.9.

Keywords: brain tissue segmentation; HMRF method; WOA; classification

Citation: Daoudi, A.; Mahmoudi, S. Enhancing Brain Segmentation in MRI through Integration of Hidden Markov Random Field Model and Whale Optimization Algorithm. *Computers* **2024**, *13*, 124. https://doi.org/10.3390/computers13050124

Academic Editors: M. Ali Akber Dewan and Selene Tomassini

Received: 25 March 2024
Revised: 13 May 2024
Accepted: 15 May 2024
Published: 17 May 2024

1. Introduction

In the human body, the most complex organ is the brain. It is responsible for coordinating and controlling many bodily activities and every process that regulates the body. Alzheimer's disease, epilepsy, encephalitis, meningitis, and brain abscesses and tumors are different forms of brain disease [1].

In recent years, the manual examination and interpretation of images obtained from various imaging modalities such as Radiography, Magnetic Resonance Imaging (MRI), and Computed Tomography (CT) have become challenging and intensive processes. This underscores the fact that that automatic image analysis by several operations is a necessity [2–4]. MRI brain segmentation helps in detecting brain diseases, analyzing brain changes, identifying pathological areas, and measuring and visualizing the anatomical structures of the brain. Furthermore, brain segmentation is a difficult task due to the homogeneities and correlations of image intensity among brain tissues. Nevertheless, many research methodologies have been proposed for brain tissue MR image segmentation. For example, Qaiser Mahmood et al. [5] present a fully automatic unsupervised segmentation algorithm called BAMS, where a combination of the Bayesian method and Adaptive Mean-Shift (BAMS) are applied to real multimodal MR images to segment brain tissues into four regions: White Matter (WM), Gray Matter (GM), Cerebrospinal Fluid (CSF), and background. In the

last step, the authors used the voxel-weighted kmeans clustering algorithm to merge the homogeneous regions obtained in the previous steps.

In another work, Henri A. Vrooman et al. [6] proposed a brain segmentation process based on an automatically trained kNN classifier. This kNN classification method incorporates voxel intensities from a T1-weighted MRI scan and a FLAIR sequence scan. In [7], the authors introduced a hybrid approach based on techniques for brain MRI segmentation. The method utilizes the Gabor transform for computing features of brain MRI. Subsequently, these features are subjected to classification using various classifiers, including Incremental Supervised Neural Network, K-NN, Probabilistic Neural Network (PNN), and Support Vector Machine (SVM). A drawback of these approaches [5–7] is that they may give poor tissue classifications in the presence of noise, and that they are computationally expensive.

In recent years, there has been more research in the field of brain tumor MR image segmentation. For example, the study of Jalab H A et al. [8] presented and evaluated a novel convolutional neural autoencoder designed for brain tumor segmentation using semantic segmentation principles. The evaluation was conducted on a dataset consisting of 3064 T1-weighted Contrast-Enhanced Magnetic Resonance Images. In [9], Hasan AM et al. used three techniques to precisely pinpoint the area of pathological tissues in volumetric MRI brain scans: the first one is a three-dimensional active contour model without boundaries, the second one is a multi-layer perceptron neural network adopted as a classifier, and the third one is a bounding box-based genetic algorithm. The most important limitations that make brain tumor segmentation [8,9] a challenging task are the varieties of the shape and intensity of tumors, along with the probability of inhomogeneity within tumorous tissue.

The Hidden Markov Random Field Model is a segmentation algorithm popularly used in image segmentation, such as by Ahmadvand et al. [10], Jianhua et al. [11], Shah Saurabh [12], and Mingsheng Chen [13]. A combination of fuzzy clustering and the MRF model was presented by Mingsheng Chen et al., where the Fuzzy C-Means (FCM) algorithm was combined with the MRF model to filter the effect of noise and to increase the integrity of segmented regions. An additional work using the HMRF model for segmenting brain tissue was presented by Alansary et al. [14], in which the authors proposed the unsupervised learning of different brain structures from T1-weighted MR brain images, by using the Maximum A posteriori Probability (MAP) estimate with a joint Markov–Gibbs Random Field Model (MGRF). In [15], the authors proposed the optimization of the MRFM by using the Broyden–Fletcher–Goldfarb–Shanno algorithm to segment brain tissues. In [16], a generalization of the HMRF model with the Expectation Maximization (EM) method was applied and tested on brain MRI data. These hybrid methods are used to significantly decrease computational time in comparison to classical MRF. However, they often lack accurate segmentation of MRI brain tissue.

Some other studies used a Fuzzy C-Means algorithm to improve the segmentation accuracy of brain images. For example, in [17], the authors used an improved multi-view FCM with an adaptive learning mechanism to segment brain images.

In some references, brain segmentation methods based on deep learning techniques have been proposed in brain segmentation, such as by Zhao L et al. [18], Brudfors Mikael et al. [19], and Bento M [20]. For example, Lee B et al. [21] introduced a non-overlapping patch-wise U-net architecture to remedy the drawbacks of the conventional U-Net with greater retention of local information. On the other hand, Renukadevi [22] et al. proposed a medical image classification with a Histogram and Time–Frequency Differential Deep Learning method using brain Magnetic Resonance Imaging. First, a supervised training method was applied by an intensity-oriented Histogram to prepare the feature extraction step. Then, time and frequency factors were applied to the pre-processed features to obtain a set of features. These features are used in the Differential Deep Learning process. The main drawback of these approaches is their expensive computational cost, as the training process needs to be repeated multiple times. Other researchers have used hybrid approaches combining deep learning with fuzzy logic to segment MRI brain tumors. For example, in [23], the authors propose a novel approach combining fuzzy

logic-based edge detection and U-Net CNN classification for brain tumor detection. This work demonstrates superior performance in identifying meningioma and non-meningioma brain images, outperforming existing methods in terms of performance metrics. But the analysis provided in this work lacks a detailed analysis of the drawbacks associated with the fuzzy logic-based edge detection or U-Net CNN classification methods used for the brain tumor detection process.

Among the optimization algorithms that have appeared in the 1980s used in images segmentation, we can cite metaheuristics methods. In the study proposed in [24], a biologically inspired ant colony algorithm was proposed to optimize the thresholding technique for MR brain image segmentation, but the thresholding methods faced some limitations that decreased the overall accuracy of the segmentation method. On the other hand, Thuy Xuan Pham et al. [25] presented an optimization method that combines metaheuristic methods (cuckoo search and particle swarm optimization algorithms) and an HMRF model to provide brain tissue segmentation. The authors of this work applied their model to both simulated and real MR images. This method is limited by its tendency to increase computational complexity due to the problem of selecting an appropriate value for the parameter β, as well as the running time for both the ICS and IPSO algorithms.

On the other hand, many techniques have been proposed suggested to aid in detecting brain lesions and diseases. The authors in [26] have proposed a pre-trained U-Net encoder–decoder system to extract ischemic stroke lesions (ISLs), using image processing techniques on brain MRI slices from the ISLES2015 database. This study achieved high Jaccard, Dice, and accuracy values on a dataset of 500 images. However, the main limitation of this approach is that the number of test images may not fully represent the variability in ischemic stroke lesions and increasing the training dataset size may introduce biases or artifacts in the segmentation process. Ramya, J et al. [27] present a novel method for Alzheimer's disease classification using MRI data. This method focuses on image processing techniques such as 2D Adaptive Bilateral Filtering, the ECLAHE algorithm for image enhancement, and feature extraction using GLCM and PCA. The paper lacks comparisons with other advanced classification techniques, and the proposed method presents high computational complexity. Rangaraju et al. [28] introduce a novel deep learning-based method for automated Alzheimer's disease detection using 3D brain MRI data, where the authors used a Patch Convolutional Neural Network and Octave convolution for feature identification and spatial redundancy reduction. The limitation of this method is that the accuracy metric may not be adequate for evaluating the model's efficacy if the dataset has an uneven distribution of classes.

In this proposal, our concern is to solve the problem of segmenting brain MR images into three tissues: GM, WM, and CSF, without apparent disease. To attain this objective, the whale optimization algorithm (WOA) is employed to optimize the HMRF model, offering an automated segmentation tool for brain MR images. Then, the proposed method performance evaluation is achieved on ground truth images from the BrainWeb and Internet Brain Segmentation Repository (IBSR) databases, using the Dice coefficient metric (DC) and the Jaccard coefficient (JC).

The overall contributions of this paper are as follows:

- A new optimization method applied to MRI image segmentation.
- A novel technique using the combination of HMRF and the WOA is proposed.
- The proposed method improves the accuracy of segmenting brain images into three tissues: GM, WM, and CSF.
- This manuscript primarily focuses on brain tissue segmentation to aid experts and radiologists.

The efficacy of the HMRF-WOA is tested on six datasets with various parameters collected from BrainWeb and the IBSR. The experimental results demonstrate remarkable performance when segmenting different types of homogeneous and heterogeneous tissues. By employing this architecture, our aim is to achieve improved accuracy, efficiency, and reliability compared to existing state-of-the-art models.

This paper is organized as follows: In Sections 2 and 3, we give a detailed explanation of the HMRF model and Whale Optimization Algorithm. The algorithm design (HMRF-WOA) is presented in Section 4, followed by the experimental results and discussions in Section 5, and the conclusion in the last section.

2. Hidden Markov Random Field Model

The Hidden Markov Random Field model is a stochastic process whose state sequence can be indirectly deduced from observations. The MRF includes a set of random variables. Let y be the observed image (i.e., the image for segmentation) and x the hidden image (i.e., the resulting segmented image). Both images (y and x) are formed of L sites or positions set; we note these sites as S = {s_1, s_2. . ., s_L}.

So, we consider that $y = \{y_1, y_2, \ldots, y_L\}$ is the image to be segmented, where y_s is one of the pixel values and $x = \{x_1, x_2, \ldots, x_L\}$ is the resulting segmented image, where x_s is one of the pixel classes. We consider Ey = {0. . . 255} and Ex = {1. . . K} to be the gray-level intensity space and the discrete space, respectively, where K denotes the number of homogeneous zones in the image. In classification methods, pixels are organized based on these gray levels. The random variables $Y = (y_1 \ldots, y_L)$ and $X = (x_1, \ldots, x_L)$ adopt their values from Ey and Ex, respectively.

We propose to use the HMRF model to segment the image y by searching for the optimal realization x* of X by maximizing the posteriori probability value $P[X = x/Y = y]$.

$$x^* = argmax\{P[X = x/Y = y]\}, x \in E_x \tag{1}$$

which is written by the law of Bayes:

$$P(X = x \ / \ Y = y) = \frac{P(Y = y \ / \ X = x) \ .P(X = x)}{P(Y = y)} \tag{2}$$

where $P(Y = y/X = x)$ indicates the probability distribution of $Y = y$; given that $X = x$ has occurred, it is called likelihood. $P(X = x)$ is the preliminary probability of $X = x$ based on prior knowledge. The denominator $P(Y = y)$ is the probability of $Y = y$ occurring; it is called the evidence.

For each site, we associated a descriptor which represents a gray level. Any family V(s) possessing the following properties was labelled as a neighborhood system:

- Where $s \notin V(s) \Leftrightarrow$, a site is not a neighborhood to itself.
- Where $s \in V(t) \Leftrightarrow t \in V(s)$, the neighborhood relationship is symmetrical.

The most frequently used neighborhoods are either the four or the eight nearest neighbors: they are referred to as the first- and second-order neighborhoods, respectively. The neighborhood relationship between sites is the clique $c \in C$. (C represents the set of all potential cliques.)

A Random Field X is identical to a Gibbs distribution (Hammersley–Clifford theorem) [29] if the joined probability distribution is:

$$P(X = x) = W^{-1} \ exp(-H(X = x)) \tag{3}$$

where $W^{-1} = \sum_x \exp(-H(X = x))$ is a normalization function, also called the partition function, and H is a nearly constant energy which decomposes into the sum of potential U_c functions associated with cliques $c \in C$.

$$H(X = x) = \sum_{c \in C} U(X_C) \tag{4}$$

Equation (3) becomes:

$$P(X = x) = \frac{exp(U(X_C))}{\sum_{c \in C} exp(U(X_C))} \tag{5}$$

In the image space, we take the second-order neighborhood system as the interactions system between pixels (i.e., 8 neighbors of each pixel), so we have 8 cliques for each pixel. A pair of neighboring pixels (i, j), defined as a clique potential, is used as a factor in the energy function $U(X_c)$ of the Potts model [30]. In this Potts model, the energy function is generally based on the interactions between neighboring pixels, and the formula for this energy function for image segmentation using this Potts model is written as:

$$U_c(x_i,\ x_j) = \beta\left(1 - V(x_i, x_j)\right) \tag{6}$$

where i and j are indices of the neighboring pixels.

β is a weight associated with the pair of neighboring pixels (a constant).

x_i, x_j are the classes assigned to pixels i, j, respectively.

$V(x_i, x_j)$ is a function which equals 1 if the two pixels of the clique belong to the same class and 0 otherwise.

$$V(x_i\ , x_j) = \begin{cases} 1 & if \quad x_i = x_j \\ 0 & if \quad x_i \neq x_j \end{cases} \tag{7}$$

The fundamental assumption of the HMRF model is that for any configuration x of X, the random variables Y are conditionally independent, and the distribution of the pixels follows the normal law, i.e., there is an independence between classes, and the field of observations can be modeled by the following function:

$$P(Y = y\ /\ X = x) = \prod_{s \in S} P(Y_s = y_s\ / X_s = x_s) \tag{8}$$

Given that $P(Y_s = y_s\ / X_s = x_s)$ follows the Gaussian distribution, it can be written as:

$$P(Y_s = y_s\ / X_s = x_s) = \frac{1}{\sqrt{2\pi\sigma_{x_s}^2}} \exp\left[\frac{-\left(y_s - \mu_{x_s}\right)^2}{2\sigma_{x_s}^2}\right] \tag{9}$$

where μ_{x_s} is the mean and σ_{x_s} is the standard deviation.

According to Equations (8) and (9), we obtain:

$$P(Y = y\ /\ X = x) = \prod_{s \in S} \frac{1}{\sqrt{2\pi\sigma_{x_s}^2}} \exp\left[\frac{-\left(y_s - \mu_{x_s}\right)^2}{2\sigma_{x_s}^2}\right]$$

With

$$\frac{1}{\sqrt{2\pi\sigma_{x_s}^2}} = \exp\left(ln\left(\frac{1}{\sqrt{2\pi\sigma_{x_s}^2}}\right)\right) \qquad and \quad \ln\left(\frac{1}{\sqrt{2\pi\sigma_{x_s}^2}}\right) = -\ln\left(\sqrt{2\pi\sigma_{x_s}^2}\right)$$

Then, we obtain

$$P(Y = y\ /\ X = x) = \prod_{s \in S}\left(\exp\left(-\ln\left(\sqrt{2\pi\sigma_{x_s}^2}\right)\right).\exp\left[\frac{-\left(y_s - \mu_{x_s}\right)^2}{2\sigma_{x_s}^2}\right]\right)$$

$$P(Y = y\ /\ X = x) = \prod_{s \in S} \exp\left(-\ln\left(\sqrt{2\pi\sigma_{x_s}^2}\right) - \frac{\left(y_s - \mu_{x_s}\right)^2}{2\sigma_{x_s}^2}\right)$$

$$P(Y = y\ /\ X = x) = \exp\left[-\left[\sum_{s \in S}\left[\ln\left(\sqrt{2\pi\sigma_{x_s}^2}\right) + \frac{\left(y_s - \mu_{x_s}\right)^2}{2\sigma_{x_s}^2}\right]\right]\right]$$

We come back to Bayes' law in Equation (2), with $P(Y = y)$ being the constant value C, and obtain:

$$P(X = x \ / \ Y = y) = \frac{1}{C}\exp\left[-\left[\sum_{s\in S}\left[\ln\left(\sqrt{2\pi\sigma_{x_s}^2}\right) + \frac{(y_s - \mu_{x_s})^2}{2\sigma_{x_s}^2}\right]\right]\right].\exp\left[\beta\sum_{c\in C}[1 - V(x_i, x_j)]\right]$$

$$P(X = x \ / \ Y = y) = C'.\exp\left[-\left[\sum_{s\in S}\left[\ln\left(\sqrt{2\pi\sigma_{x_s}^2}\right) + \frac{(y_s - \mu_{x_s})^2}{2\sigma_{x_s}^2}\right]\right]\right].\exp\left[\beta\sum_{c\in C}[1 - V(x_i, x_j)]\right]$$

$$P(X = x \ / \ Y = y) = C'.\exp\left[-\left[\sum_{s\in S}\left[\ln\left(\sqrt{2\pi\sigma_{x_s}^2}\right) + \frac{(y_s - \mu_{x_s})^2}{2\sigma_{x_s}^2}\right]\right] + \beta\sum_{c\in C}[1 - V(x_i, x_j)]\right]$$

$$\begin{cases} P(X = x \ / \ Y = y) = C'.\exp(-\varphi(x, y)) \\ \varphi(x, y) = \sum\limits_{s\in S}\left[\ln\left(\sqrt{2\pi\sigma_{x_s}^2}\right) + \frac{(y_s - \mu_{x_s})^2}{2\sigma_{x_s}^2}\right] + \beta\sum\limits_{c\in C}[1 - V(x_i, x_j)] \end{cases}$$

where C' is a positive constant and β is used to control the size of homogeneous regions and the interaction between their sites. μ_{x_i}, σ_{x_i} are the mean and standard deviation of the class x_i, respectively (i.e., the ith region $\Omega_i = \{s \ / \ x_s = i\}$ in the image). Then, μ_{x_i}, σ_{x_i} are described as follows:

$$\begin{cases} \mu_i = \frac{1}{|\Omega_i|}\sum_{s\in\Omega_i} y_s \\ \sigma_i = \sqrt{\frac{1}{|\Omega_i|}\sum_{s\in\Omega_i}(y_s - \mu_i)} \end{cases} \quad (10)$$

Once we know all the parameters of the HMRF model, we can perform the segmentation itself, i.e., find the value to maximize the probability $P(X = x/Y = y)$, which is equivalent in this context to minimize $\varphi(x, y)$ such that $x^* = \text{argmin}\ \{\varphi(x, y)\}$.

To seek a given pixel class x_s, we can consider an approximation of the exact segmentation using optimization techniques. Furthermore, we can obtain the optimal segmentation $x^*(x_1, \ldots x_s \ldots x_L)$ through μ^* $(\mu_1, \ldots \mu_i, \ldots, \mu_k)$ by classifying y_s into the same category of the nearest mean μ_i of μ (i.e., $x_s = i$ if the nearest mean of y_s is μ_i). We seek μ^* instead of x^* and the optimal means value μ^* as follows:

$$\mu^* = \text{argmin}\{\varphi(\mu)\} \quad (11)$$

where $\varphi(\mu)$ is defined as:

$$\varphi(\mu) = \sum_{s\in S}\left[\ln\left(\sqrt{2\pi\sigma_{x_s}^2}\right) + \frac{(y_s - \mu_{x_s})^2}{2\sigma_{x_s}^2}\right] + \beta\sum_{c\in C}[1 - V(x_i, x_j)] \quad (12)$$

This objective function (Equation (12)) is simply a formula that can be applied in the optimization process. Accordingly, in the section below, we will define the optimization method applied in this work.

3. Whale Optimization Algorithm

The Whale Optimization Algorithm is among the latest bio-inspired optimization algorithms. It is proposed for optimizing numerical problems [31]. Humpback whales are among the largest and oldest animals in the world; they are highly intelligent animals that feel emotion and never sleep [32–34]. This algorithm emulates the intelligent foraging behavior of this animal. This hunting comportment is called the bubble net feeding method and is an exclusive method of hunting that can only be observed in humpback whales.

In recent years, a large number of works in the literature have applied the WOA for optimization in several fields, such as [35–39]. In order to perform optimization, including the exploitation and exploration phases, the mathematical model is explained below. For more details, please refer to [31,40].

Step 1: Encircling Prey phase

When the prey's location is identifiable, humpback whales start to circle their prey. Then, the humpback whales create bubble nets to catch their prey. $X_i^t = \left(x_{i,1}^t \ldots x_{N,D}^t\right)$ denotes the place of the ith whale at time t (iteration value), with i $\in$ [1...N], where N represents the whale population and D is the dimensions of the problem. In the search zone, the whales consider the target prey or prey in the close vicinity as the optimal solution; during this phase, other whales seek to come closer to the best search agent and update their position using Equation (13).

$$D = |C.X^*(t) - X_i(t)| \tag{13}$$

$$\mathrm{X}_i(\mathrm{t}+1) = X^*(t) - A.D \tag{14}$$

where t indicates the present iteration, the parameter $X_i(t)$ denotes the position of each individual i at the tth iteration, $X^*(t)$ signifies the optimal global position at the tth iteration, and $|\,|$ is the absolute value. Equations (15) and (16) are used to define the factor vectors A and C, respectively:

$$A = 2ar - a \tag{15}$$

$$\mathrm{C} = 2\mathrm{r} \tag{16}$$

$$\mathrm{a} = 2.\left(1 - \frac{t}{T_{max}}\right) \tag{17}$$

The parameter (a) linearly declines over the course of the iteration from 2 to 0, and r is a random value in [0, 1].

Step 2: Bubble-Net Attacking Method (Exploitation Phase)

Two mechanisms are designed to mathematically model the predation behavior of humpback whales, which can be described as follows:

1. Shrinking encircling mechanism: According to Equation (15), the decrease in the value of A depends on the decrease in the value of the control parameter a. Note that the search agent approaches the current optimal solution when the value of the random variable A is set in the range $[-1, 1]$.
2. Spiral updating position: To capture food, humpback whales take a spiral-shaped path around their prey. Equations (18) and (19) are used to reproduce the helix-shaped movement of humpback whales and to calculate the distance between the whale and the prey, respectively:

$$X_i(t+1) = D'.\, e^{bl}.\cos(2\pi.l) + X^*(t) \tag{18}$$

$$D' = |X^*(t) - X_i(t)| \tag{19}$$

where D' is the distance between the whale and prey (the best solution obtained so far), b is a constant that defines the logarithmic shape, and l is a random value in $[-1, 1]$. During the iterations of the algorithm, the movement behavior of humpback whales is either shrinking encircling or spiral movement. For this behavior, assuming a probability of 50%, the mathematical model can be described as follows:

$$X_i(t+1) = \begin{cases} X^*(t) - A.D & if \quad p < 0.5 \\ D'.\, e^{bl}.\cos(2\pi.l) + X^*(t) & if \quad p \geq 0.5 \end{cases} \tag{20}$$

where p is an arbitrary value in [0, 1].

Step 3: Search for Prey (Exploration Phase)

In the exploration phase, the search is performed randomly. First, one of the whales' populations is selected randomly to allow the global search, then according to this randomly

chosen population the position of the search is updated. In this phase, it is necessary to use the random values of the parameter A higher than 1 or lower than -1 to obligate the search agent to move far away from a reference whale. The model's equations are expressed as follows:

$$D = |C.X_{rand} - X\ | \tag{21}$$

$$X_i(t+1) = X_{rand} - A.D \tag{22}$$

where X_{rand} represents a random position vector chosen from the available whales in the population.

As mentioned earlier, the Whale Optimization Algorithm (WOA) is one of the latest swarm-based algorithms and it showed high performance when addressing various optimization problems, such as an analysis of medical image segmentation [41] and optimization tasks [42]. Recently, the WOA gained significant attention from researchers due to its ability to be quickly implemented and its requirement of only a few parameters to fine-tune [43]. The simplicity of this method and its success in solving some optimization problems attracted our attention to employ it to address MRI brain segmentation problems.

The WOA depends on the initial values of the population obtained by a set of random solutions. First, the WOA takes the initial values randomly, whereas, during iterations, the search agents optimize their positions accorded by the randomly selected search agent or based on the current optimal solution. The current solution is calculated according to the fitness function values as the optimal solution. To apply this algorithm and track its steps, a new hybrid method was proposed to solve the optimization issues called HMRF-WOA, a proposed hybrid algorithm that links the steps of the WOA with the HMRF model. The HMRF-WOA is depicted in the next section.

4. HMRF and Whale Optimization Algorithm (HMRF-WOA)

This section explains the connection between the Hidden Markov Random Field Model and the Whale Optimization Algorithm. As discussed in Section 2, MRF is one of the most effective methods for achieving image segmentation of images using the maximum a posterior (MAP) criterion. However, due to some problems such as noise, overlapping regions, and low contrast in medical images, MRF seems to be inadequate. Moreover, in order to accurately identify the class of a given pixel, we can consider an approximation of the exact segmentation using optimization techniques. In addition, to seek a given pixel class, we can consider an approximation of the exact segmentation using optimization techniques. For these reasons, we employed WOA as an optimizing tool to aid in segmenting MR brain images. WOA is utilized to define the optimal class of pixel in brain MR images.

Therefore, by combining MRF- and WOA-based methods, we can leverage the advantages of both techniques to significantly improve the accuracy of segmentation and also to address issues related to low contrast in MRI images. Additionally, we can achieve optimal segmentation by considering the mean and standard deviation of each class. So, pixels are classified into the same category as the nearest mean, and during the algorithm iterations, the best solution is selected based on the fitness function values (Equation (12)) referenced in Section 2. This objective function serves to quantify the proximity of a solution to the optimal solution.

Moreover, the brain tissue segmentation problem can be solved by the HMRF-WOA method, where the objective function given in Equation (12) can converge or close in on the optimal solution. The HMRF-WOA initiates using a random value of the populations with predefined search elements ($X_1 \ldots X_i \ldots X_n$), and each one has a set of predefined value of the initial locations $X_i = (X_{i1}, \ldots X_{ij} \ldots X_{\mathrm{ik}})$. Through the iterations of the algorithm, we calculated, for each search agent i, the new position by the fitness function, obtaining a set of positions for all populations and conserving the best set of positions.

Let $\mu_i(\mathrm{t}) = (\mu_{i1}(\mathrm{t}), \ldots, \mu_{ij}(\mathrm{t}), \ldots, \mu_{ik}(\mathrm{t}))$ be the best location visited by the search agent i until the time t calculated by the fitness function, which allows us to define its own resulting

segmented image $x_i(t) = (x_{i1}(t),\ldots,x_{is}(t),\ldots,x_{iM}(t))$ by using its location $\mu_i(t)$, where $x_{is}(t) = j$, on the condition that the mean $\mu_{ij}(t)$ is nearest to y_s. After identifying the optimal search element by its best position μ_i, other search elements will adjust their positions towards the best search element. Consequently, the best position obtained by the population thus far is $\mu = (\mu_1, \ldots, \mu_i, \ldots \mu_k)$.

Our proposed segmentation method of brain MRIs by the HMRF-WOA has the following main steps (Algorithm 1).

Algorithm 1: The main steps of our proposed segmentation method of brain MRIs by the HMRF-WOA.

Input: Initialize randomly a population X_i

Initialization of the search elements (agents X_i) and i = 1, 2. . .n.
For each element i, compute the fitness value by Equation (12).
X* designed the best search element.
  Do while (t $\leq$ number of iterations) is true.
    For each i in the population of the search agents
      These parameters (a, A, C, l, and p) are updated.
      If ($p < 0.5$)
        If (| A | < 1)
          The current search agent's position is updated by Equation (14)
        Else if (i.e., | A | $\geq$ 1)
          A random search agent (Xrand) is selected.
          The current search agent's position is updated by Equation (22).
        End if
      Else if (i.e., $p \geq 0.5$)
      The current search agent's position is updated by Equation (18).
      End if
    End for
  Check that if any search agent exceeds the boundaries of the search space and make the correction.
  Recompute the fitness value of all the population (each search agent) by Equation (12).
  Getting better solution, update X*.
  Increment the iteration (t).
  End while

Output: The optimal solution is X*.

5. Experimental Results

In this part of the manuscript, we will explain the segmentation method results in detail. Our proposed method is a hybrid algorithm that links the HMRF model and the WOA metaheuristic algorithm, called HMRF-WOA, and our goal is to classify each pixel of the brain tissues into four categories: WM, GM, CSF, and background. To obtain this result, firstly, we applied the median filter to reduce noise with a structure of [3 $\times$ 3] and to improve the segmentation results to achieve a high quality. Then, we started our proposed HMRF-WOA process to research each region in the image and obtain its optimal mean intensity.

One of the most successful research approaches is acquiring appropriate data for testing the proposed methods, which often presents a major challenge for researchers, especially in studies related to the human body. BrainWeb provides a valuable resource for the research community by offering a set of realistic simulated brain MR image volumes (Simulated Brain Database, SBD) with reference data (ground truth). These databases are particularly suitable for brain tissue research. For this reason, we have chosen these datasets as they offer a sufficient amount of data for brain image segmentation and are highly appropriate for our purpose.

5.1. Datasets

In this experimental phase, we chose two datasets of the MR images, including both T1-weighted simulated and real 2D MRI brain images. The Simulated Brain Database (SBD) was downloaded from the BrainWeb database [44], which can be accessed at this link (https://brainweb.bic.mni.mcgill.ca/brainweb/), accessed on 20 October 2022. On the one hand, we have five BrainWeb databases with different input image parameters. Table 1 below contains all these parameters.

Table 1. The parameters of the databases used in the proposed method.

Databases	Types	Dimensions	Noises (%)	INU * (%)	Voxels (mm)
1	Brainweb	181 × 217 × 181	0	0	1 × 1 × 1
2	Brainweb	181 × 217 × 181	3	20	1 × 1 × 1
3	Brainweb	181 × 217 × 181	5	20	1 × 1 × 1
4	Brainweb	181 × 217 × 181	7	20	1 × 1 × 1
5	Brainweb	181 × 217 × 181	9	40	1 × 1 × 1
6	IBSR	256 × 256 × 63	-	-	1 × 3 × 1

* Intensity non-uniformity = INU.

On the other hand, the real MR images with T1-weighted modality, known as the Internet Brain Segmentation Repository (IBSR), were collected from the 20 normal MR brain datasets, which are available at (https://www.nitrc.org/projects/ibsr/), accessed on 20 October 2022, where the input image parameters were dimensions = 256 × 256 × 63 and voxels = 1 × 3 × 1 mm. In totality, six datasets with various parameters were considered as input data to apply our algorithm.

5.2. Performance Measures

With the purpose of interpreting the HMRF-WOA's performance, this manuscript uses two measures which are most often used in the evaluation of medical volume segmentation: the Dice coefficient metric (DC) [45] and the Jaccard coefficient (JC) [46].

5.2.1. Dice Coefficient (Dice)

This is a metric based on overlap that directly evaluates the similarity between a segmented image and a ground truth image. If the value of DC equals or is close to 1, this indicates the best performance of the method.

$$Dice = \frac{2.\ area\ of\ overlap}{total\ area} = \frac{2.TP}{2.TP + FP + FN} \tag{23}$$

5.2.2. Jaccard Coefficient (JC)

JC is an evaluation index that summarizes the area of overlap between two groups of binary segmentations. This metric is defined as the ratio of intersection over union of the ground truth image and the resulting segmented image. A higher result of this metric signifies a better result. The JC index is defined as follows:

$$JC = \frac{area\ of\ overlap}{area\ of\ union} = \frac{TP}{TP + FP + FN} \tag{24}$$

where TP, FP, and FN are the true positive, the false positive, and the false negative, respectively.

Furthermore, the parameter called β in the fitness function (Equation (12)) can influence the performance of the algorithm. In this case, it is necessary to fix the coefficient β when the weights present a part of the energy of the model. We chose $\beta = 1$ in this work. Table 1 defines the different databases used in our proposed method.

5.3. Discussion

The accuracy of any segmentation method depends on several factors, including the choice of the proposed technique, and a number of its parameters, such as the dataset, number of regions to be segmented or classified, the number of iterations, and the workstation configuration. Within this framework, we have achieved superior segmentation results compared to other methods (see Tables 2–4). This is due to the use of prior knowledge.

Table 2. Mean DC values of the simulated MR brain images (BrainWeb).

Tissue	Method	Database 1	Database 2	Database 3	Database 4	Database 5
GM	HMRF-WOA	0.982	0.974	0.953	0.955	0.935
	HMRF-BFGS	0.973	0.942	0.918	NA *	NA *
	MV-FCM	0.885	0.876	0.866	0.854	0.836
	Amiri et al. [47]	0.975	0.960	0.930	0.925	0.895
	AWSFCM	NA *	0.895	0.836	0.809	NA *
	WMT-FCM	NA *	0.9508	0.9219	0.8818	NA *
WM	HMRF-WOA	0.997	0.990	0.986	0.986	0.976
	HMRF-BFGS	0.991	0.969	0.951	NA *	NA *
	IMV-FCM	0.952	0.950	0.938	0.929	0.918
	Amiri et al. [47]	0.960	0.950	0.920	0.920	0.880
	AWSFCM	NA *	0.865	0.836	0.813	NA *
	WMT-FCM	NA *	0.9729	0.9550	0.9306	NA *
CSF	HMRF-WOA	0.979	0.977	0.951	0.952	0.968
	HMRF-BFGS	0.960	0.939	0.919	NA *	NA *
	IMV-FCM	0.850	0.844	0.837	0.870	0.813
	Amiri et al. [47]	0.970	0.960	0.940	0.930	0.925
	AWSFCM	NA *	0.692	0.672	0.658	NA *
	WMT-FCM	NA *	0.9628	0.9424	0.9090	NA *

* The performance of the method for this tissue was not reported.

Table 3. Mean JC values of simulated MR brain images from BrainWeb.

Tissue	Method	Database 1	Database 2	Database 3	Database 4	Database 5
GM	HMRF-WOA	0.966	0.944	0.925	0.916	0.879
	HMRF-BFGS	NA *	NA *	NA *	NA *	NA *
	IMV-FCM	0.797	0.781	0.765	0.753	0.722
	Amiri et al. [47]	0.959	0.920	0.880	0.860	0.820
	AWSFCM	NA *	0.787	0.742	0.726	NA *
WM	HMRF-WOA	0.995	0.987	0.977	0.973	0.953
	HMRF-BFGS	NA *	NA *	NA *	NA *	NA *
	IMV-FCM	0.904	0.892	0.877	0.858	0.835
	Amiri et al. [47]	0.925	0.915	0.870	0.850	0.800
	AWSFCM	NA *	0.760	0.743	0.721	NA *

Table 3. *Cont.*

Tissue	Method	Database 1	Database 2	Database 3	Database 4	Database 5
CSF	HMRF-WOA	0.961	0.949	0.927	0.914	0.939
	HMRF-BFGS	NA *	NA *	NA *	NA *	NA *
	IMV-FCM	0.707	0.679	0.670	0.675	0.718
	Amiri et al. [47]	0.925	0.920	0.920	0.885	0.860
	AWSFCM	NA *	0.520	0.516	0.485	NA *

* The performance of the method for this tissue was not reported.

Table 4. Mean DICE coefficient values of MR brain images from the IBSR.

Tissue	Method	Mean Dice
GM	HMRF-WOA	0.916
	hMRF-BFGS	0.859
	PLA-SOM	0.780
	Amiri et al. [47]	0.863
	Gardens2	0.740
	KPSFCM	0.80
WM	HMRF-WOA	0.856
	hMRF-BFGS	0.855
	PLA-SOM	0.740
	Amiri et al. [47]	0.814
	Gardens2	0.720
	KPSFCM	0.81
CSF	HMRF-WOA	0.459
	hMRF-BFGS	0.381
	PLA-SOM	0.230
	Amiri et al. [47]	0.423
	Gardens2	0.230
	KPSFCM	0.31

As mentioned before, the images of the first five datasets in Table 3 were used to evaluate the performance of the HMRF-WOA. Figures 1–5 show some slices of a T1-weighted image (slices: 84, 95, 105, 108, 120). These brain images correspond to the slices under different types of conditions, such as database type, dimension image, noise level, intensity non-uniformity level, and slice thickness (mm). In Table 1, rows 1 to 5 summarize the parameters of Figures 1–5, respectively. Figure 6 represents the ground truth segmentation of slices 84, 95, 105, 108, and 120. In this figure, each column contains the three tissues, GM, WM, and CSF, of each slice. Figures 7–11 show the segmentation results, where the four tissues (BG, GM, WM, and CSF) are shown with different colors. The yellow, red, and green colors represent the segmented regions of GM, WM, and CSF, respectively. As we can also see from these figures, the resulting segmented images in Figures 7–11 are almost close to the initial images in Figures 1–5.

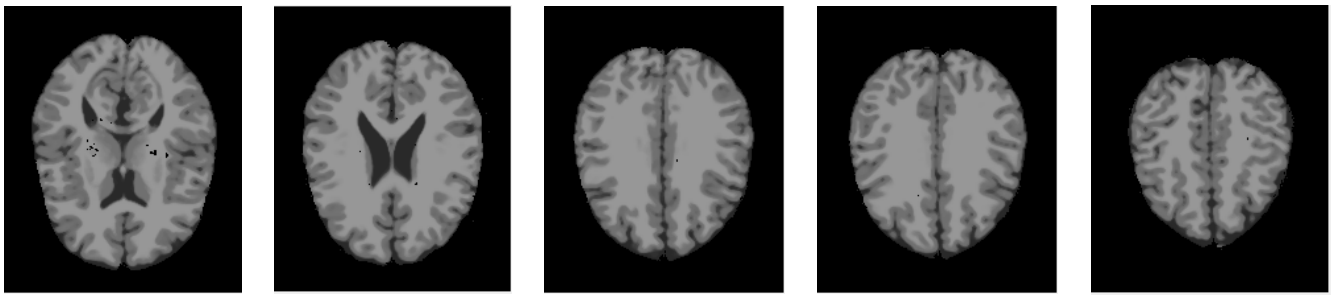

Figure 1. Slices with Noise = 0%, INU = 0% of database 1.

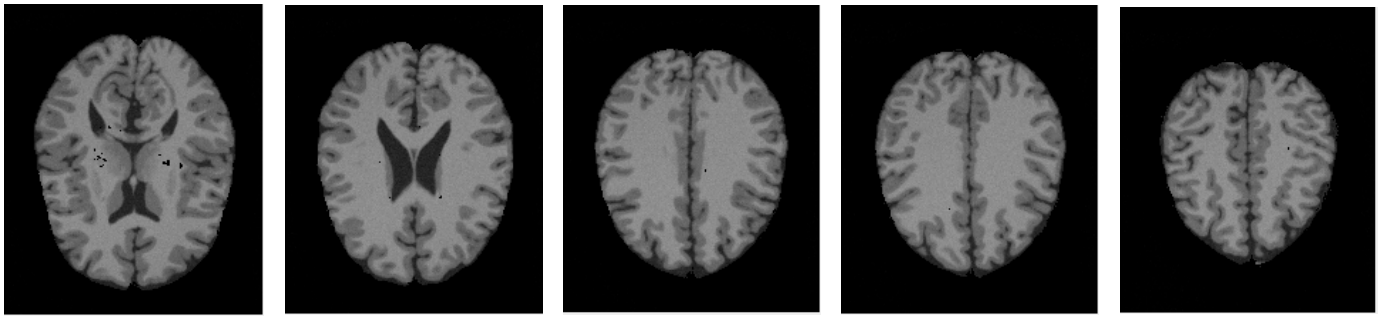

Figure 2. Slices with Noise = 3%, INU = 20% of database 2.

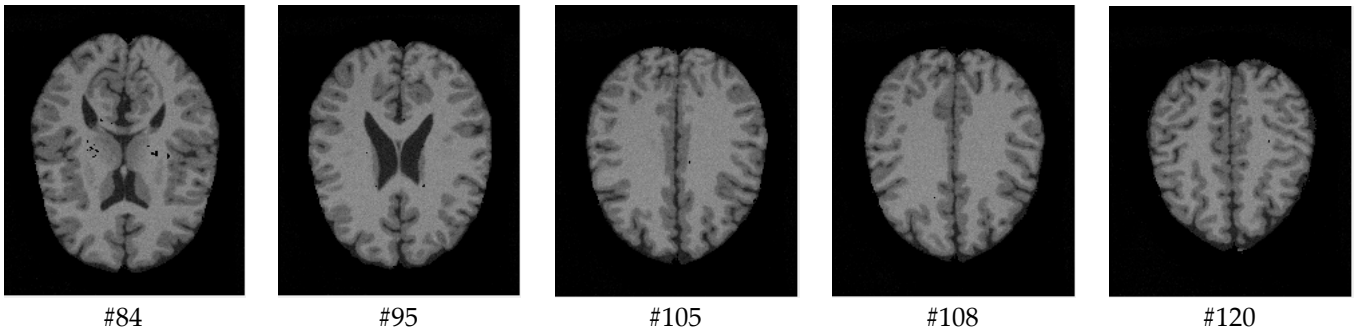

Figure 3. Slices with Noise = 5%, INU = 20% of database 3.

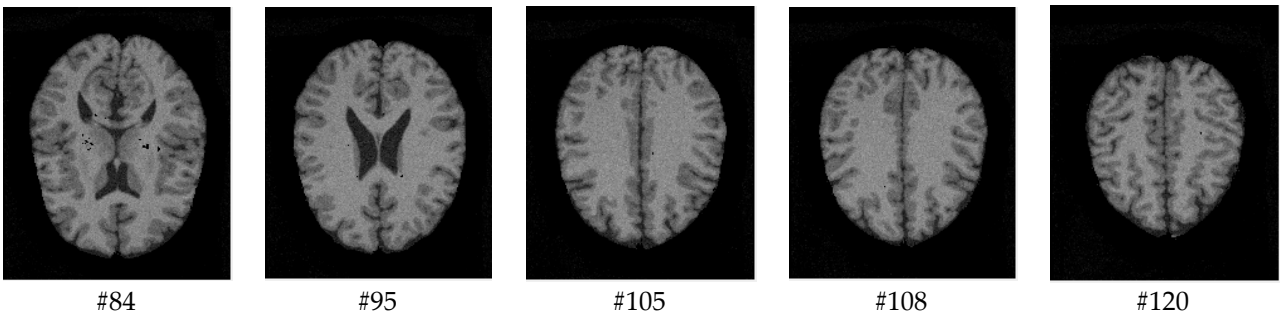

Figure 4. Slices with Noise = 7%, INU = 20% of database 4.

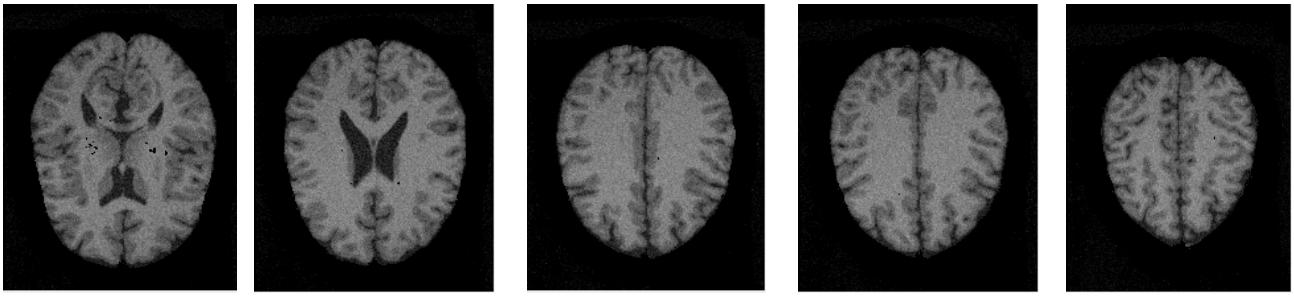

Figure 5. Slices with Noise = 9%, INU = 40% of database 5.

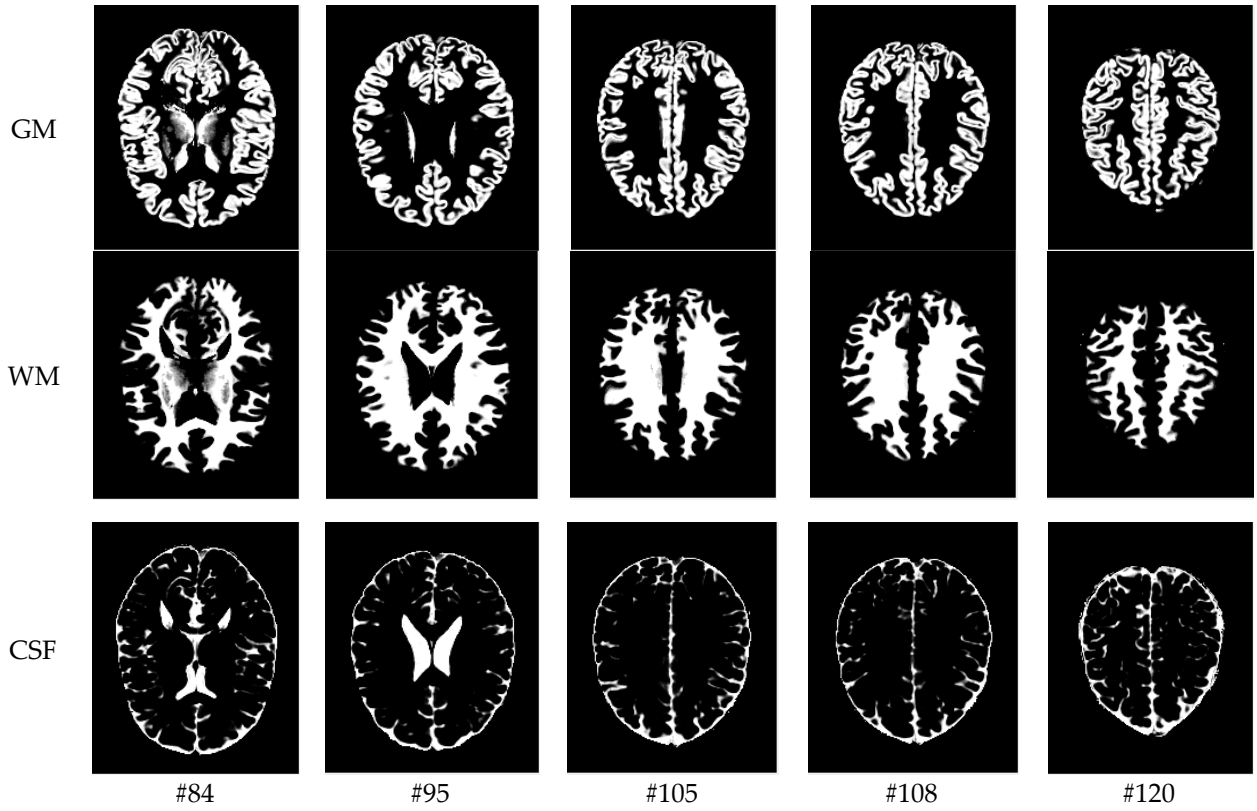

Figure 6. Ground truth segmentation of the GM, WM, and CSF tissues.

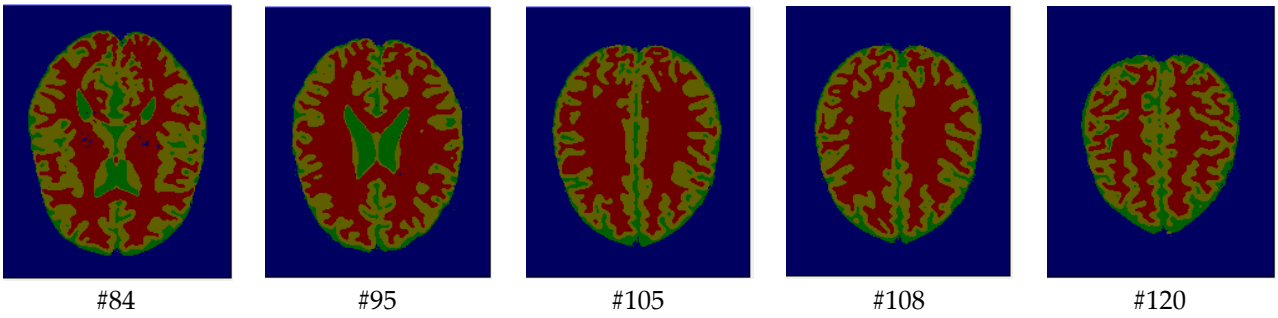

Figure 7. Segmentation results of the slices illustrated in Figure 1.

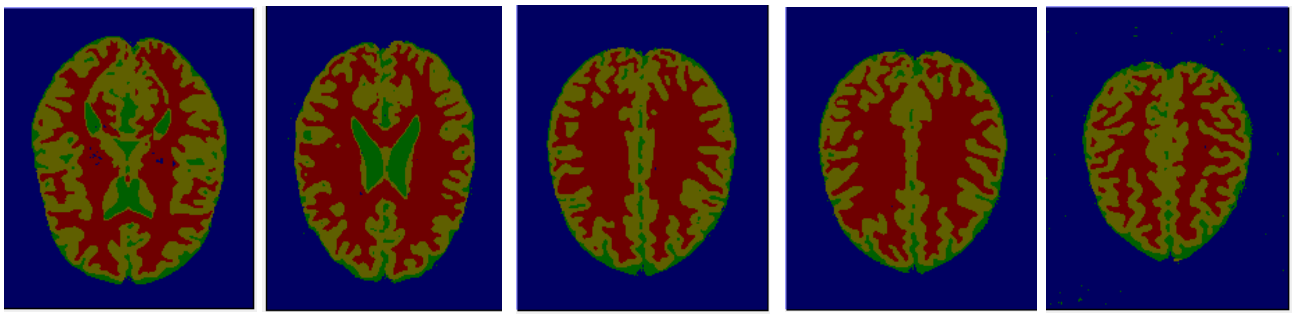

Figure 8. Segmentation results of the images illustrated in Figure 2.

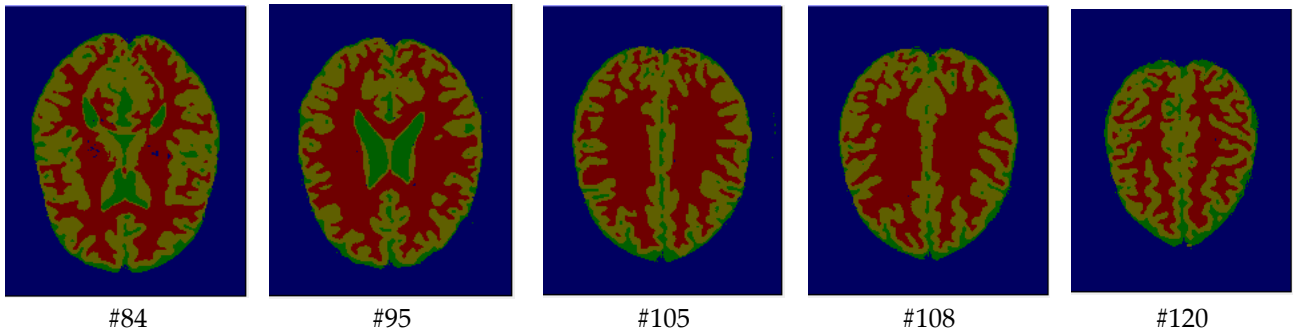

Figure 9. Segmentation results of the images illustrated in Figure 3.

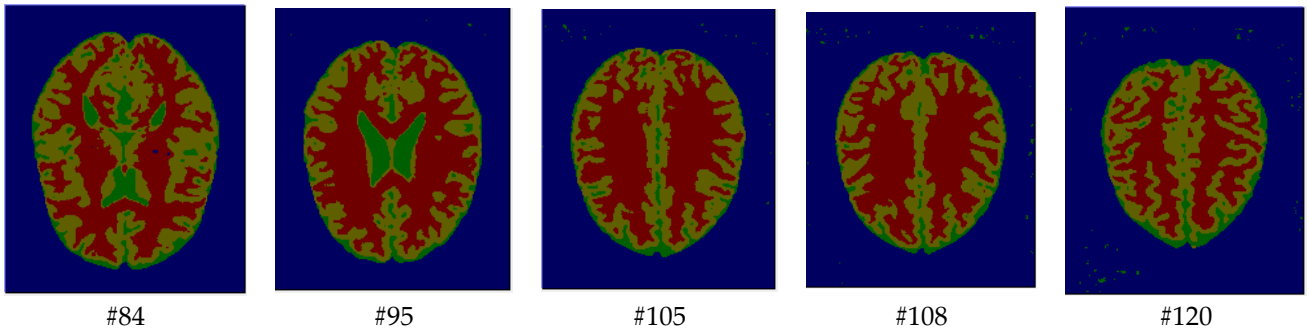

Figure 10. Segmentation results of the images illustrated in Figure 4.

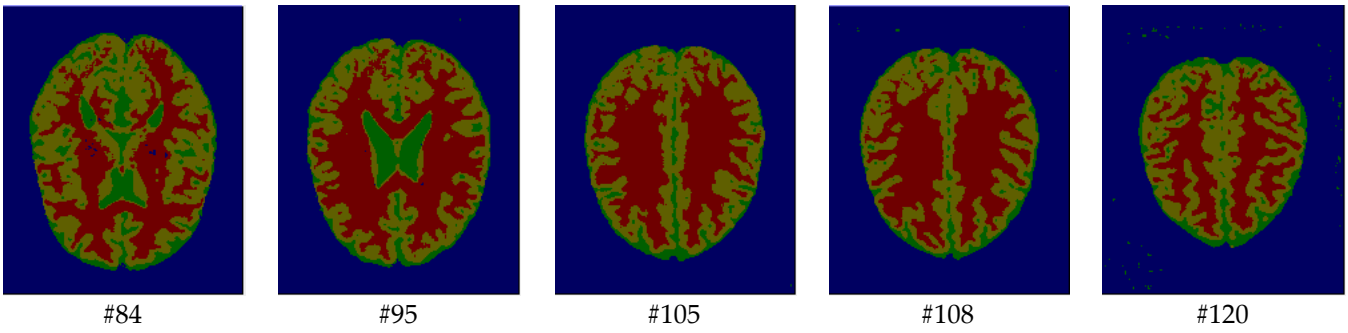

Figure 11. Segmentation results of the images illustrated in Figure 5.

Hence, we have demonstrated the high performance of our method, despite existing artifacts on the MR brain images. To evaluate the performances of the HMRF-WOA more clearly, two criteria were used to compare the similarities between the manual (GT) and automatic segmentations: DC and AC, which are described in the previous section.

The results are summarized in Tables 2 and 3. Moreover, Figures 12–17 illustrate the comparison of the DC and JC coefficients between five approaches: HMRF-BFGS, IMV-FCM, Amiri et al. [47], AWSFCM [48], WMT-FCM [49], and HMRF-WOA. According to these figures, the test results show that the present approach brings satisfactory results compared with the literature methods for all brain tissues.

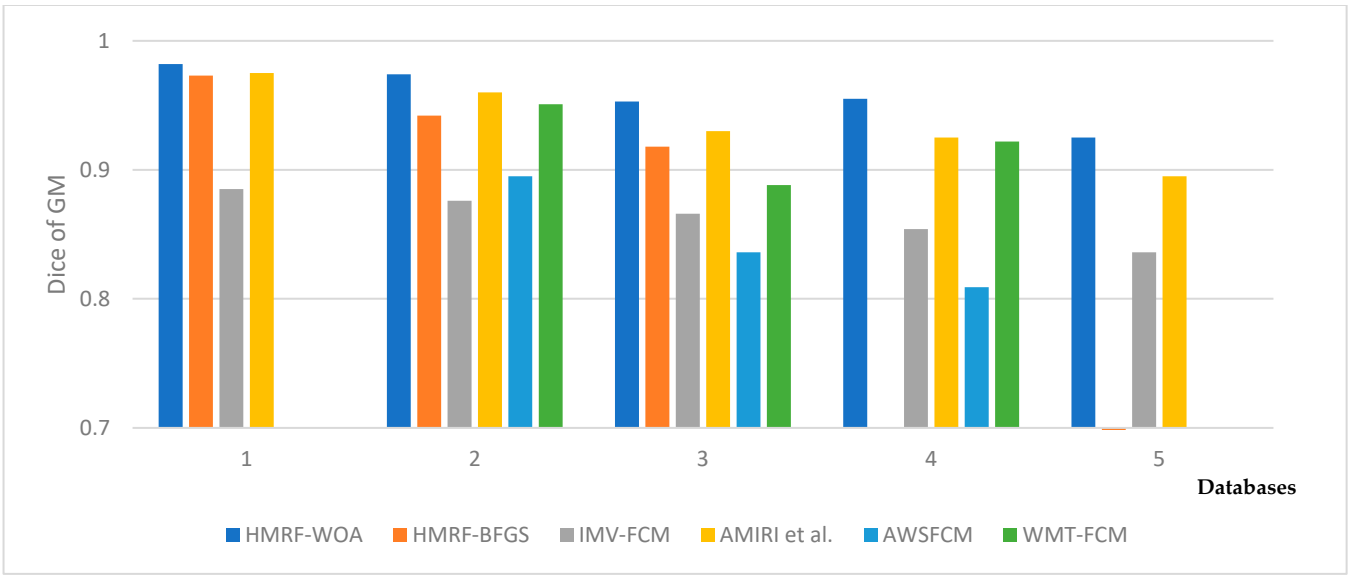

Figure 12. Dice coefficient of GM (BrainWeb dataset) for each algorithm [47].

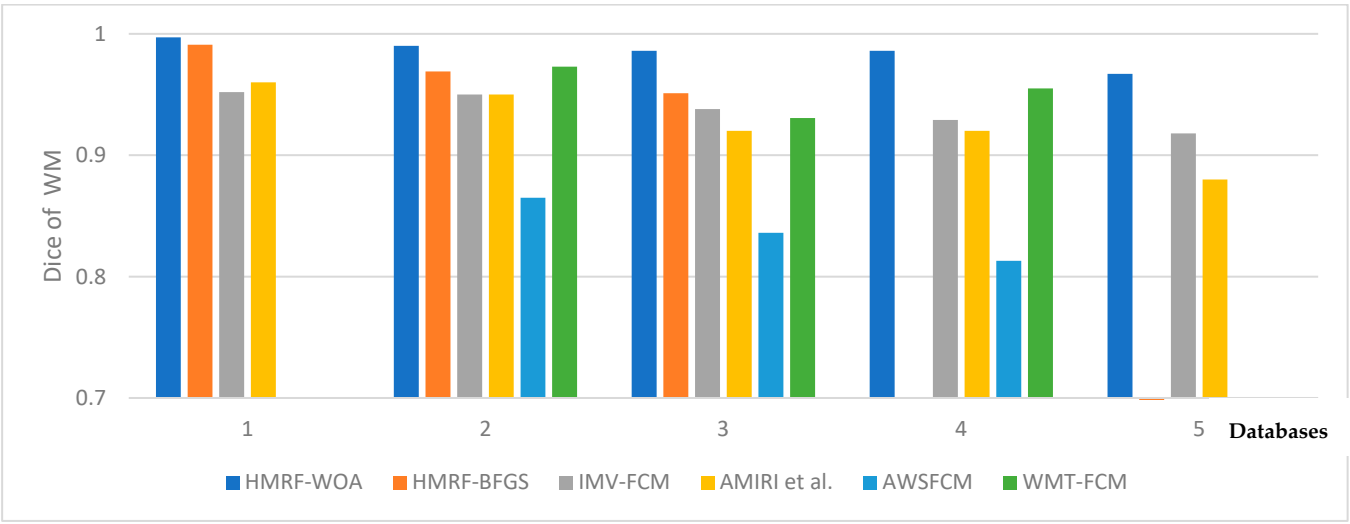

Figure 13. Dice coefficient of WM (BrainWeb dataset) for each algorithm [47].

With regard to the T1-weighted MRI brain datasets, the performance of the HMRF-WOA was evaluated for 20 normal subjects. Figure 18 shows some slices of one subject (slices 20, 28, 32, 35, and 39); Figure 18a presents the initial slices images, (b) represents the ground truth segmentation, and (c) shows the HMRF-WOA segmentation results.

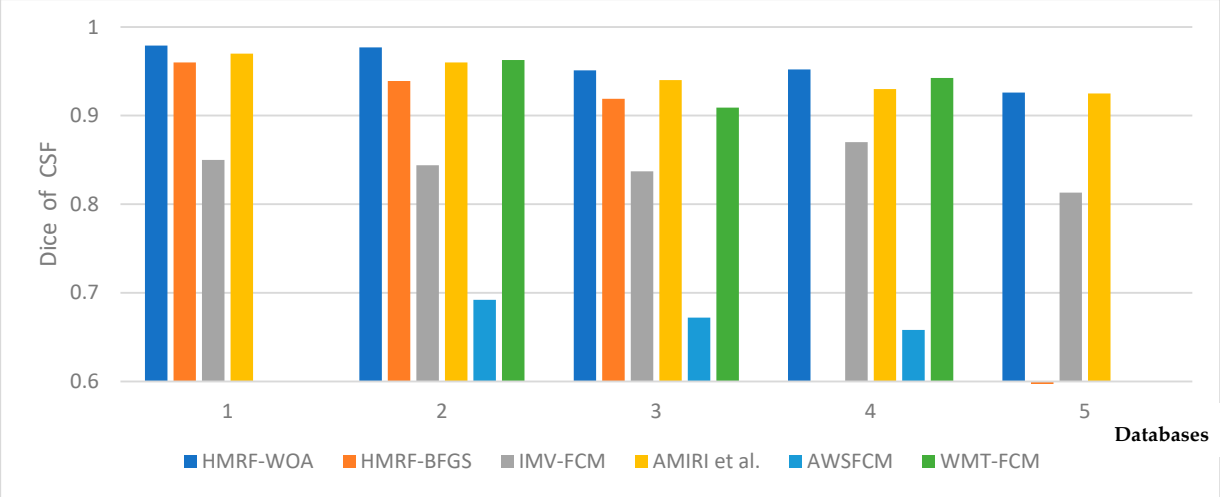

Figure 14. Dice coefficient of CSF (BrainWeb dataset) for each algorithm [47].

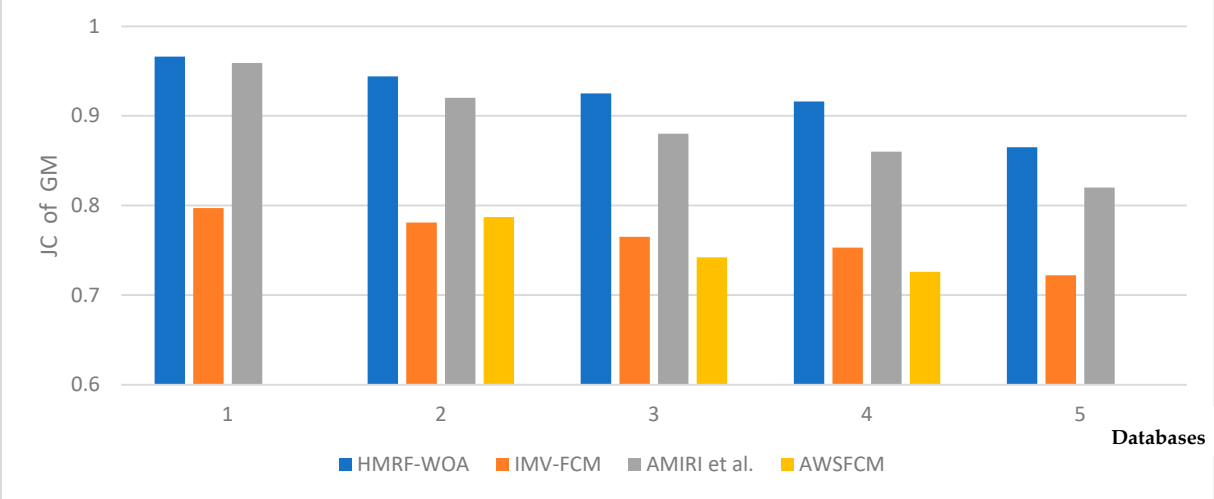

Figure 15. Jaccard coefficient of GM (BrainWeb dataset) for each algorithm [47].

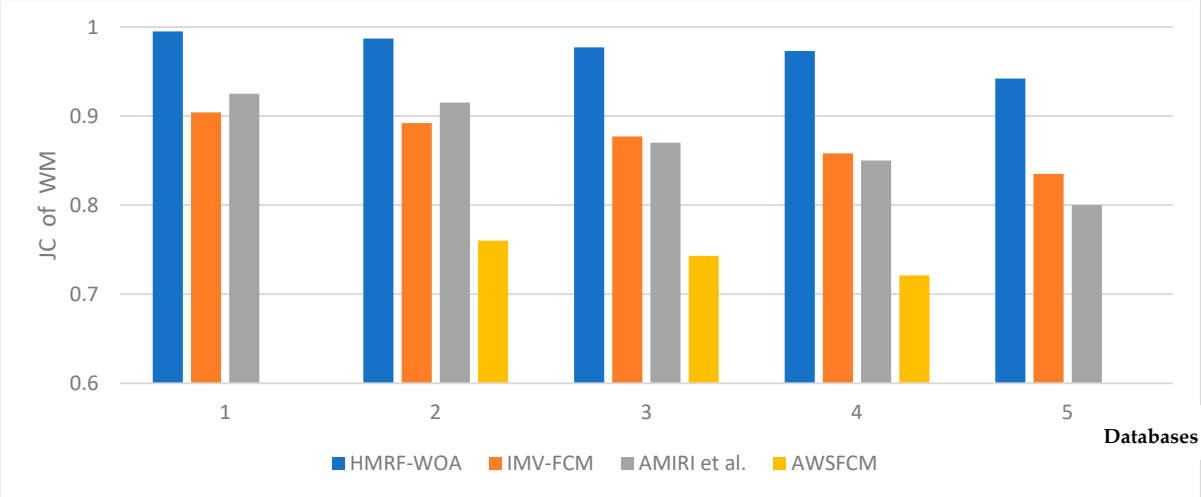

Figure 16. Jaccard coefficient of WM (BrainWeb dataset) for each algorithm [47].

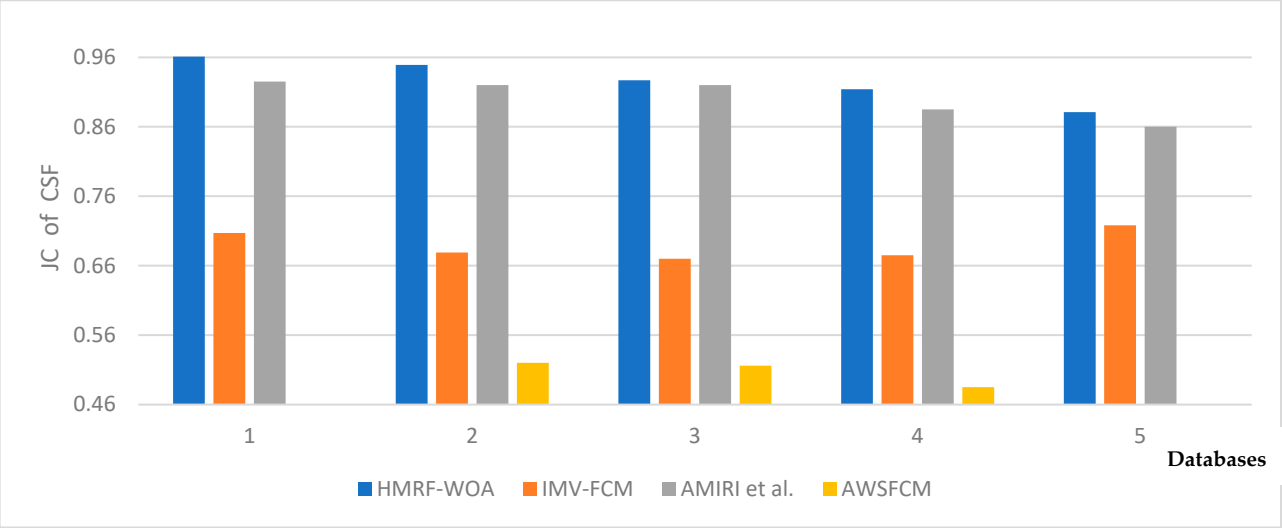

Figure 17. Jaccard coefficient of CSF (BrainWeb dataset) for each algorithm [47].

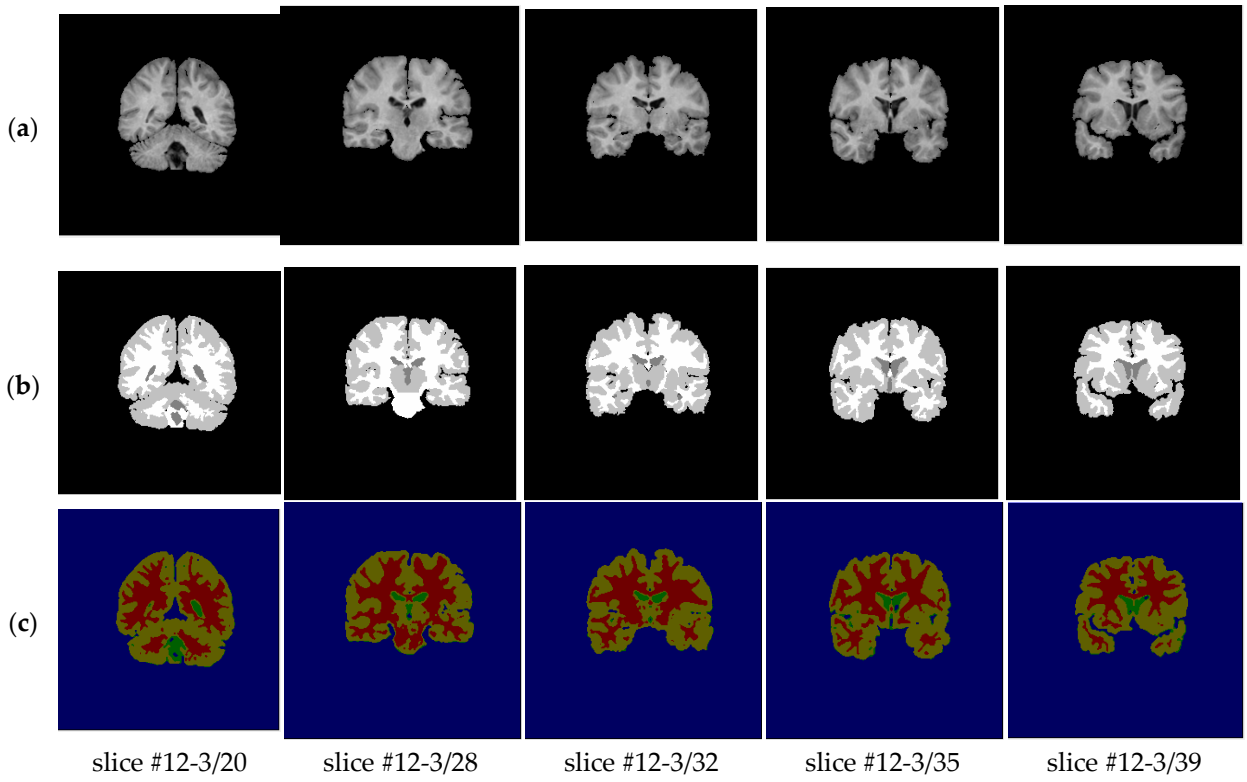

Figure 18. Segmentation results of IBSR dataset: (**a**)—initial images; (**b**)—ground truth images; (**c**)—segmentation results.

Table 4 below illustrates the Mean DC values of the MR brain images from the IBSR obtained by our proposed method (HMRF-WOA) and the literature methods. In this assessment, we have added other approaches, such as PLA-SOM [50], Gardens2 [51], andKPSFCM [52], for GM, WM, and CSF segmentation. All the comparative methods shown in this table use the same database images. So, this comparison shows that the HMRF-WOA performed significantly better than the other methods.

The graphical presentation of the mean DC index for the three tissues (CSF, WM, and GM) between our proposed method and the literature methods is shown in Figure 19. This comparison shows that the average DC index of the GM and CSF segmentations is

strongly improved in the IBSR dataset. On the other hand, the average DC indexes of the WM segmentations between our method and hMRF-BFGS suggests that the improvement is slight.

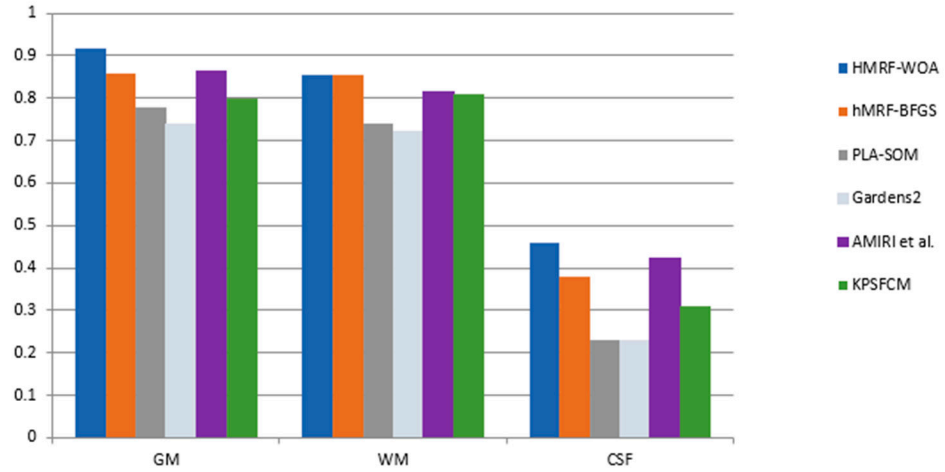

Figure 19. Mean DC of brain tissues in IBSR dataset [47].

As shown, these analyses confirmed the accuracy and the robustness of our automatic method. In addition, the proposed method, called HMRF-WOA, outperforms the literature methods used for our comparison.

The qualitative analysis provides a visual representation of the segmentation approaches. The visual comparison of the resulting images using the HMRF-WOA appears to be more similar to the reference image (ground truth), where Figures 1–5 show the GM, WM, and CSF tissue regions of the reference image with higher values of noise levels (3, 5, 7, and 9%) and intensity non-uniformity levels (20, 40%), whereas Figures 7–11 show the subject images obtained using the proposed technique. However, this result shows that with higher values of noise and intensity non-uniformity, the algorithm, with its hyperparameters, is able to segment the tissue regions correctly.

Moreover, Figure 18 illustrates the segmentation results of the proposed algorithm using MR brain images from the IBSR database. Figure 18a presents the slices of the original brain image; Figure 18b is the ground truth slice images; and Figure 18c shows the segmented brain MR images using the HMRF-WOA approach on the sample image of one subject. GM is shown in yellow, WM in red, CSF in green, and the background in blue.

Therefore, these analyses confirmed the accuracy and the robustness of our automatic method. In most cases, we achieved acceptable results using these brain datasets.

In this framework, the HMRF-WOA incorporates three hyperparameters:

1. The weight β associated with the pair of neighboring pixels is a positive constant that controls the size of homogeneous regions. Also, increasing the value of the β parameter e can increase the contribution of the neighboring sites in the estimation of the class of a given pixel. So, we chose $\beta = 1$ as we obtained a good performance for the segmentation method using this value.
2. The whale population size parameter represents the total number of whales used in the WOA to optimize the MRI image segmentation. We have tested three values of this parameter (10, 20, and 30). Using 20 search agents gave the best accuracy result and a good computational cost compared to other values.
3. The number of iterations represents the number of loops used to evaluate the HMRF-WOA process. We tested values ranging between 5 and 40 iterations. The best result was obtained with 20 iterations.

The choice of these parameters shows its effect on the performance of the HMRF-WOA.

Computational Complexity Analysis

Computing time serves as a crucial measure for justifying the computational effectiveness of any method. Our proposed approach with these hyperparameters showed a good efficiency and a better performance compared to other segmentation methods. However, a notable drawback of this method is its computational complexity. A critical limitation arises from the selection of hyperparameters, where the balance between computational cost and accurate results must be carefully considered. Another limitation is that we have not tested the algorithm's performance to evaluate its generalizability on other MRI types or imaging modalities.

In addition to this, the computational complexity of the algorithm is computed as follows:

1. Initializing the whale population is $O(N)$, where N is the size of the population.
2. Computing the fitness value of the initial population is $O(N)$.
3. Obtaining the best solution is $O(N^2)$.
4. Iteration, updating whale population, and evaluating fitness are $O(2N)$.
5. Iteration and obtaining the best solution are $O(N^2)$.

Therefore, the total time complexity of HMRF-WOA is:

$$O(2N) + O(N^2) + maxiter\ (O(2N) + O(N^2)) == (maxiter + 1)\ (O(N^2 + 2N))$$

where *maxiter* is the maximum number of iterations used as the termination criteria for the algorithm.

6. Conclusions

Efficient methods of segmentation and classification are some of the most challenging tasks for physicians and radiologists. The automation of these methods thus occupies a major proportion of research in the domain of medical imaging.

The motive of medical image processing for handling human organs is to precisely segment or classify the tissue regions to make operations easier.

In this study, a novel combination of the HMRF model and a whale optimization algorithm (WOA) are applied to segment the images of two well-known brain datasets: BrainWeb and IBSR. We conclude that our HMRF-WOA outperforms all the other methods or techniques compared in this study, where the assessment results of the segmented tissues as illustrated in all the figures indicate that the HMRF-WOA can precisely segment the brain tissues at different noise levels, despite the presence of the intense inhomogeneity in the input images. Overall, comparing the proposed method with the results of other techniques shows that the method can yield an acceptable result for GM, WM, and CSF segmentation. The results are summarized in Tables 2 and 3.

This increased robustness and accuracy of our HMRF-WOA optimization method-based MRI brain segmentation technique will hopefully help the application of MR image segmentation techniques, such as measuring the anatomical structures measurement of the brain, surgical planning, and image-guided interventions.

In the future, we would like to hybridize the WOA method with other techniques to show their main benefits and to achieve higher performances in the treatment process.

Author Contributions: Conceptualization, A.D.; Methodology, A.D.; Software, A.D.; Validation, A.D.; Supervision, S.M. All authors have read and agreed to the published version of the manuscript.

Funding: This research received no external funding.

Institutional Review Board Statement: Not applicable.

Data Availability Statement: All data were contained in the main text.

Conflicts of Interest: The authors declare no conflict of interest.

References

1. Falaq, N.; Yasir, S. Human brain disorders: A Review. *Open Biol. J.* **2020**, *8*, 6–21. [CrossRef]
2. Catalina, T.G.; Geers, A.J.; Peters, J.; Weese, J.; Pinto, K.; Karim, R.; Ammar, M.; Daoudi, A.; Margeta, J.; Sandoval, Z.; et al. Benchmark for Algorithms Segmenting the left atrium from 3D CT and MRI datasets. *IEEE Trans. Med. Imaging* **2015**, *34*, 1460–1473. [CrossRef] [PubMed]
3. Abdelaziz, D.; Said, M.; Chikh, M. Automatic segmentation of the left atrium on CT images. In *Statistical Atlases and Computational Models of the Heart. Imaging and Modelling Challenges. STACOM 2013*; Springer: Berlin/Heidelberg, Germany, 2014; Volume 8330, pp. 14–23. [CrossRef]
4. Abdelaziz, D.; Said, M.; Chikh, M. Automatic Segmentation of the Right Ventricle by Active Shape Model and a Distance Transform. *JMIHI J. Med. Imaging Health Inform.* **2015**, *5*, 27–35. [CrossRef]
5. Qaiser, M.; Alipoor, M.; Chodorowski, A.; Mehnert, A.; Persson, M. Multimodal MR Brain segmentation using Bayesian based Adaptive Mean-Shift. *MIDAS J.* **2013**. [CrossRef]
6. Henri, A.V.; Fedde, V.; Wiro, J. Auto knn: Brain tissue segmentation using automatically trained k-nearest-neighbor classification. *MIDAS J.* **2011**. [CrossRef]
7. Fiaz, M.; Ali, K.; Rehman, A.; Gul, M.J.; Jung, S.K. Brain MRI Segmentation using rule-based hybrid approach. *arXiv* **2019**, arXiv:1902.04207. [CrossRef]
8. Jalab, H.A.; Hasan, A.M. Magnetic resonance imaging segmentation techniques of brain tumors: A Review. *Arch. Neurosci.* **2019**, *6*, e84920. [CrossRef]
9. Hasan, A.M.; Meziane, F.; Aspin, R.; Jalab, H. Segmentation of Brain Tumors in MRI Images using three-dimensional active contour without edge. *Symmetry* **2016**, *8*, 132. [CrossRef]
10. Ahmadvand, A.; Yousefi, S.; Manzuri, M. A novel markov random field model based on region adjacency graph for T1 magnetic resonance imaging brain segmentation. *IJIST Int. J. Imaging Syst. Technol.* **2017**, *27*, 78–88. [CrossRef]
11. Jianhua, S.; Lei, Y. Brain tissue segmentation via non-local fuzzy c-means clustering combined with markov random field. *MBE Math. Biosci. Eng.* **2021**, *19*, 1891–1908. [CrossRef]
12. Shah, S.A.; Chauhan, N.C. An automated approach for segmentation of Brain MR Images using gaussian mixture model based Hidden Markov Random Field with Expectation Maximization. *BJHMR Br. J. Healthc. Med. Res.* **2015**, *2*, 57. [CrossRef]
13. Chen, M.; Yan, Q.; Qin, M. A segmentation of brain MRI images utilizing intensity and contextual information by Markov random field. *Comput. Assist. Surg.* **2017**, *22*, 200–211. [CrossRef] [PubMed]
14. Alansary, A.; Soliman, A.; Khalifa, F.; Elnakib, A.; Mostapha, M.; Nitzken, M.; Casanova, M.; El-Baz, A. MAP Based framework for segmentation of MR Brain Images based on visual appearance and prior shape. *MIDAS J.* **2014**. [CrossRef]
15. Elhachemi, G.; Samy, A.; Dominique, M.; Ramdane, M. Hidden markov random field model and broyden fletcher goldfarb shanno algorithm for brain image segmentation. *JETAI J. Exp. Theor. Artif. Intell.* **2017**, *30*, 415–427. [CrossRef]
16. Castillo, D.; Peis, I.; Martínez, F.; Segovia, F.; Górriz, J.; Ramírez, J.; Salas, D. A Heavy tailed expectation maximization hidden markov random field model with applications to segmentation of MRI. *Front. Neurosci.* **2017**, *11*, 66. [CrossRef]
17. Hua, L.; Gu, Y.; Gu, X.; Xue, J.; Ni, T. A novel brain MR image segmentation method using an improved multi view fuzzy c-means clustering algorithm. *Front. Neurosci.* **2021**, *15*, 662674. [CrossRef]
18. Zhao, L.; Asis-Cruz, J.D.; Feng, X.; Wu, Y.; Kapse, K.; Largent, A.; Quistorff, J.; Lopez, C.; Wu, D.; Qing, K.; et al. Automated 3D fetal brain segmentation using an optimized deep learning approach. *AJNR Am. J. Neuroradiol.* **2022**, *43*, 448–454. [CrossRef]
19. Brudfors, M.; Balbastre, Y.; Ashburner, J.; Rees, G.; Nachev, P.; Ourselin, S.; Cardoso, M.J. An MRF Unet product of experts for image segmentation. In Proceedings of the Machine Learning Research, Proceedings of the Fourth Conference on Medical Imaging with Deep Learning, Lübeck, Germany, 7–9 July 2021; ML Research Press: Westminster, UK, 2021; Volume 143, pp. 48–59.
20. Bento, M.; Fantini, I.; Park, J.; Rittner, L.; Frayne, R. Deep learning in large and multi site structural brain MR imaging datasets. *Front. Neuroinform.* **2022**, *15*, 805669. [CrossRef] [PubMed]
21. Lee, B.; Yamanak, K.; Nagaraj, M.; Muhammad, A.; Choi, J. Automatic segmentation of brain MRI using a novel patch-wise U net deep architecture. *PLoS ONE* **2022**, *17*, e0264231. [CrossRef]
22. Renukadevi, T.; Saraswathi, K.; Prabu, P.; Venkatachalam, K. Brain image classification using time frequency extraction with histogram intensity similarity. *CSSE Comput. Syst. Sci. Eng.* **2022**, *41*, 645–660. [CrossRef]
23. Maqsood, S.; Damasevicius, R.; Shah, F.M. An Efficient Approach for the Detection of Brain Tumor Using Fuzzy Logic and U-NET CNN Classification. In *Computational Science and Its Applications—ICCSA*; Lecture Notes in Computer Science; Springer: Cham, Switzerland, 2021; pp. 105–118. [CrossRef]
24. Khorram, B.; Yazdi, M. A New optimized thresholding method using ant colony algorithm for MR brain image segmentation. *J. Digit. Imaging* **2019**, *32*, 162–174. [CrossRef] [PubMed]
25. Thuy, X.; Patrick, S.; Hamouche, O. Segmentation of MR Brain images through Hidden Markov Random Field and hybrid metaheuristic algorithm. *IEEE Trans. Image Process.* **2020**, *29*, 6507–6522. [CrossRef] [PubMed]
26. Kadry, S.; Damaševičius, R.; Taniar, D.; Rajinikanth, V.; Lawal, I.A. U-Net Supported Segmentation of Ischemic-Stroke-Lesion from Brain MRI Slices. In Proceedings of the Seventh International Conference on Bio Signals, Images, and Instrumentation (ICBSII), Chennai, India, 25–27 March 2021; pp. 1–5. [CrossRef]

27. Ramya, J.; Maheswari, B.U.; Rajakumar, M.P.; Sonia, R. Alzheimer's Disease Segmentation and Classification on MRI Brain Images Using Enhanced Expectation Maximization Adaptive Histogram (EEM-AH) and Machine Learning. *Inf. Technol. Control.* **2022**, *51*, 786–800. [CrossRef]
28. Rangaraju, B.; Chinnadurai, T.; Natarajan, S.; Raja, V. Dual Attention Aware Octave Convolution Network for Early-Stage Alzheimer's Disease Detection. *Inf. Technol. Control.* **2024**, *53*, 302–316. [CrossRef]
29. Clifford, P.; Hammersley, J. *Markov Fields on Finite Graphs and Lattices*; University of Oxford: Oxford, UK, 1971.
30. Potts, R. Some generalized order-disorder transformations. *Math. Proc. Camb. Philos. Soc.* **1952**, *48*, 106–109. [CrossRef]
31. Mirjalili, S.; Lewi, A. The whale optimization algorithm. *AES Adv. Eng. Softw.* **2016**, *95*, 51–67. [CrossRef]
32. Goldbogen, J.; Friedlaender, A.; Calambokidis, J.; McKenna, M.; Malene, S.; Nowacek, D. Integrative approaches to the study of baleen whale diving behavior, feeding performance, and foraging ecology. *BioScience* **2013**, *63*, 90–100. [CrossRef]
33. Hof, P.; Gucht, E. Structure of the cerebral cortex of the humpback whale, megaptera novaeangliae (Cetacea, Mysticeti, Balaenopteridae). *Anat. Rec.* **2007**, *290*, 1–31. [CrossRef] [PubMed]
34. Watkins, W.; Schevill, W.E. Aerial Observation of feeding behavior in four baleen whales: Balaena glacialis, balaenoptera borealis, Megaptera novaeangliae, and Balaenoptera physalus. *J. Mammal.* **1979**, *60*, 155–163. [CrossRef]
35. Nasiri, J.; Khiyabani, F.M.; Yoshise, A. A whale optimization algorithm (WOA) approach for clustering. *CMS Cogent Math. Stat.* **2018**, *5*, 1483565. [CrossRef]
36. Yue, Y.; You, H.; Wang, S.; Cao, L. Improved whale optimization algorithm and its application in heterogeneous wireless sensor networks. *IJDSN Int. J. Distrib. Sens. Netw.* **2021**, *17*. [CrossRef]
37. Mohammed, A.K.; Suhaib, A.A.; Zakariya, Y.A. Improving whale optimization algorithm for feature selection with a time-varying transfer function. *NACO Numer. Algebra Control Optim.* **2021**, *11*, 87–98. [CrossRef]
38. Zhihong, Y.; Shuqian, W.; Bin, L.; Xinde, L. Application of whale Optimization Algorithm in Optimal Allocation of Water Resources. *E3S Web Conf.* **2018**, *53*, 04019. [CrossRef]
39. Reddy, P.; Reddy, V.; Manohar, T. Whale optimization algorithm for optimal sizing of renewable resources for loss reduction in distribution systems. *Renewables* **2017**, *4*, 3. [CrossRef]
40. Nadimi, S.; Zamani, H.; Asghari, V.Z.; Mirjalili, S. A Systematic Review of the Whale Optimization Algorithm: Theoretical Foundation, Improvements, and Hybridizations. *Arch. Comput. Methods* **2023**, *30*, 4113–4159. [CrossRef] [PubMed]
41. Mostafa, A.; Hassanien, A.E.; Houseni, M.; Hefny, H. Liver segmentation in MRI images based on whale optimization algorithm. *Multimed. Tools Appl.* **2017**, *76*, 24931–24954. [CrossRef]
42. Kaur, R.; Khehra, B.S. Modified Whale Optimisation Algorithm and minimum CROSS entropy-based segmentation of CT Liver image. *J. Pharm. Negat. Results* **2023**, *14*, 2908–2931.
43. Chakraborty, S.; Saha, A.K.; Nama, S.; Debnath, S. COVID-19 X-ray image segmentation by modified whale optimization algorithm with population reduction. *Comput. Biol. Med.* **2021**, *139*, 104984. [CrossRef] [PubMed]
44. Kwan, R.; Evans, A.; Pike, G. MRI simulation-based evaluation of image-processing and classification methods. *IEEE Trans. Med. Imaging* **1999**, *18*, 1085–1097. [CrossRef] [PubMed]
45. Dice, L. Measures of the Amount of Ecologic Association between Species. *Ecology* **1945**, *26*, 297–302. [CrossRef]
46. Jaccard, P. The Distribution of the Flora of the Alpine Zone. *New Phytol.* **1912**, *11*, 37–50. [CrossRef]
47. Amiri, S.; Movahedi, M.; Kazemi, K.; Parsaei, H. 3D cerebral MR image segmentation using multiple-classifier system. *Med. Biol. Eng. Comput.* **2017**, *55*, 353–364. [CrossRef] [PubMed]
48. Mishro, P.; Agrawal, S.; Panda, R.; Abraham, A. A Novel Type-2 Fuzzy C-Means Clustering for Brain MR Image Segmentation. *IEEE Trans. Cybern.* **2021**, *51*, 3901–3912. [CrossRef] [PubMed]
49. Yunlan, Z.; Zhiyong, H.; Hangjun, C.; Fang, X.; Man, L.; Mengyao, W.; Daming, S. Segmentation of Brain Tissues from MRI Images Using Multitask Fuzzy Clustering Algorithm. *JHE J. Health Eng.* **2023**, 4387134. [CrossRef] [PubMed]
50. Jonas, G.B.; Pilar, G. Pseudo Label Assisted Self-Organizing Maps for Brain Tissue Segmentation in Magnetic Resonance Imaging. *JDI J. Digit. Imaging* **2022**, *35*, 180–192. [CrossRef] [PubMed]
51. Jonas, G.B.; Pilar, G. Segmentation of MRI brain scans using spatial constraints and 3D features. *Med. Biol. Eng. Comput.* **2020**, *58*, 3101–3112. [CrossRef]
52. Padmanaban, S.; Thiruvenkadam, K.; Karuppanagounder, S.; Rangasami, R. A Rapid Knowledge Based Partial Supervision Fuzzy C Means for Brain Tissue Segmentation with CUDA Enabled GPU Machine. *IJIST Int. J. Imaging Syst. Technol.* **2019**, *29*, 547–560. [CrossRef]